



HAL
open science

Oil-water pore occupancy in the Vaca Muerta source-rocks by NMR cryoporometry

M. Fleury, T. Chevalier, R. Jorand, I. Jolivet, B. Nicot

► **To cite this version:**

M. Fleury, T. Chevalier, R. Jorand, I. Jolivet, B. Nicot. Oil-water pore occupancy in the Vaca Muerta source-rocks by NMR cryoporometry. *Microporous and Mesoporous Materials*, 2021, 311, pp.110680. 10.1016/j.micromeso.2020.110680 . hal-03137148

HAL Id: hal-03137148

<https://ifp.hal.science/hal-03137148>

Submitted on 10 Feb 2021

HAL is a multi-disciplinary open access archive for the deposit and dissemination of scientific research documents, whether they are published or not. The documents may come from teaching and research institutions in France or abroad, or from public or private research centers.

L'archive ouverte pluridisciplinaire **HAL**, est destinée au dépôt et à la diffusion de documents scientifiques de niveau recherche, publiés ou non, émanant des établissements d'enseignement et de recherche français ou étrangers, des laboratoires publics ou privés.

Oil-water pore occupancy in the Vaca Muerta source-rocks by NMR cryoporometry.

Fleury M.^a, Chevalier T.^a, R. Jorand^b, I. Jolivet^c, B. Nicot^c

^a IFP Energies nouvelles, Rueil-Malmaison, France

^b CVA Engineering, Pau, France

^c Total E&P, Pau, France

ABSTRACT

The main motivation of this work is to determine quantitatively the pore occupancy of water and oil in some source rocks. The pore occupancy might be imposed by differences in chemical composition, wettability behavior and sorption of fluids in organic and inorganic porosities and will dramatically affect the hydrocarbons flow through the porous medium. We address this issue using NMR cryoporometry in two phase situations complemented by other NMR measurements. Using oil-wet samples originating from the Vaca Muerta formation, oil saturation as large as 70% were obtained by simply immersing fully water saturated samples into decane. At 100% water saturation, the measured pore size distributions indicate two main peaks around 2 and 80 nm. After immersion into oil, the pores occupied by water in the presence of decane are mostly around 2 nm and less. The pore sizes occupied by decane in the presence of water can then be deduced by subtracting the distributions obtained at 100% water saturation and after spontaneous drainage. Oil is mainly located in pores around 80 nm. These measurements are confirmed by high resolution SEM images showing the presence of porosity in the organic matter (sponge-like structure). Most of the oil can be associated with the porous organic matter network as shown by SEM images. These observations are complemented by the determination of the porosity below 2 nm and the water connectivity. From D₂O diffusion experiments at 100% water saturation, we observed that about 19% of the total porosity is non-exchangeable with D₂O. From the measurements of the liquid signal at -29°C, we observed that on average 58% of the total porosity is located in pores smaller than 2 nm.

1 Introduction

Shales are difficult systems to characterize and have been the subject of intense and numerous research work [1]. Measurement workflows valid for conventional hydrocarbon reservoirs have to be modified [2,3] and require techniques able to reach not only the nanometer scale [4–8] but simultaneously a wide range spanning typically up to 1 μm. Although challenging to integrate over a large range of sizes, imaging techniques are essential to the understanding of the pore structure but they must be complemented by unambiguous quantitative information. The traditional mercury intrusion technique is often used for this task although limited to a few nanometers but it deeply relies on the connectivity of the porous system beside requiring a dry sample and generating potential damage to the structure. Each with a given resolution, many other techniques exist and must be combined to cover the desired range. However they must be compared carefully (see [9] for a comparison of standard techniques). For the study of shales, nitrogen adsorption curves, small angle X-ray or neutron scattering (SAXS, SANS) are often combined with high resolution scanning

electron microscopy [10,11]. In this context, NMR cryoporometry techniques (NMRC), although known for many years [12] have been used only recently in geosciences and essentially with the impulse of source rock research [11,13–16]. NMRC may solve many difficulties because a pore size distribution can be measured in a saturated state, either with water or hydrocarbons, and hence with the least disturbances to the pore structure. Two recent reviews summarizing the state of the art about this technique are available in literature [17,18]. It can be noted that the largest pore size available with standard cryoporometry devices is about 100 nm whereas the technique used in this work allows a considerable increase of this upper limit by almost one order of magnitude.

Considering all the knowledge accumulated on shales, our main objective is to get some information about the pore occupancy of oil and water in these systems and this issue has not been considered much in literature. NMR techniques are well suited to fluid typing in shales and have been intensively used in the laboratory but also in well logging [19]. In two phase situations, the interpretation of T_2 relaxation time distributions alone can be ambiguous and the use of T_1 - T_2 maps improved significantly the identification of the origin of the different proton populations among bitumen, water in clays, mobile water, oil in organic and inorganic porosity [20–23]. Wettability and the dynamics of oil and water are also of interest [24,25] since it plays a major role in production. However, contrary to natural porous media in conventional oil production, T_2 relaxation time distributions do not represent the true pore size distribution due to diffusive coupling between pores [26] and the specific location of water and oil in the pore size distribution has not been evidenced. The use of cut-off values on the T_2 distribution can help evaluating oil or gas saturation [28] but it does not give the pore size occupied by oil or gas. Hence NMRC appears as an ideal technique for our objectives but such experiments are usually not performed in the presence of two immiscible fluids. Using decane and water at various fraction, Alnaimi et al. [27] performed such experiments in a silica sample and showed the pores occupied by decane and water. The system considered had however a narrow pore size distribution centered around 10 nm. Here we consider wide pore size distributions spanning from 1nm up to 1 μm typical of shales, together with small scale heterogeneities in terms of chemical composition (various minerals, presence of organic matter).

2 Sample and methods

We provide first a brief description of the principles of the cryoporometry method and the specificity of our apparatus in single phase saturation and the extension to two phase saturation. We also describe other NMR measurements performed to complement the cryoporometry experiments.

2.1 NMR cryoporometry technique (NMRC)

The principle of cryoporometry is based on the shift of the melting temperature of a fluid when located in a pore (Gibbs-Thomson theory). A simplified form of the Gibbs-Thomson equation may be written as:

$$\Delta T_m(x) = T_m^{bulk} - T_m(x) = \frac{k_{GT}}{x} \quad (1)$$

where T_m^{bulk} is the bulk melting temperature, x is a dimension related to the pore size and k_{GT} is the so-called Gibbs-Thomson constant. In the melting cycle, it has been shown that x corresponds to a radius of curvature dV/dS [18]. In this way the melting temperature depends on liquid nature and pore size. For water at a given temperature below zero, smaller pores will melt and contain liquid instead of ice. For water, we chose the value $k_{GT} = 58.2 \text{ K}\cdot\text{nm}$ [14,29] determined using a set of well

characterized systems; hence at $x=2$ and 10 nm, water will melt respectively at -29.1 and -5.8°C . With the simplified formulation of equation 1, the constant k_{GT} contains a hidden shape factor of 2 corresponding to a cylinder. Hence if the porous system considered contains cylindrical pores, the measured pore size corresponds to a diameter.

If one detects the amount of liquid volume $V(T)$ present in the sample as a function of temperature T , one can obtain the pore size distribution $P(d)$ from the derivative of the $V(T)$ curve using the following equation [17,18]:

$$P(d) = -\frac{k_{GT}}{d^2} \cdot \frac{dV}{dT} \quad (2)$$

In equation 2, $P(d)$ has units of $\mu\text{l}/\text{nm}$. However since we plot the distributions using log scales, an appropriate representation is $P(d) \cdot d$ vs. $\ln(d)$ yielding units of μl in the graphs. The integration of the distribution P represents the amount of melted volume V_m during the heating of the sample. A Curie law correction was applied to properly evaluate all volumes from NMR magnetization measurements.

While most NMR spectrometers are equipped with an air flow system allowing to cool a sample in general down to about -50°C or less, our system uses a Peltier effect to control the temperature of the sample (Figure 1), originally designed by B. Webber [16]. A copper hollow cylinder is connected to the Peltier system in order to vary the temperature in a stable way. The NMR probe accommodates standard 5 mm diameter glass tubings in which a sample of diameter 3.9 mm in diameter and 20 mm in length can be inserted. Compared to air flow systems, it has a much better temperature homogeneity and resolution, a high thermal inertia, has no nitrogen consumption and is easy to control and program. At the present time the temperature in the sample is limited to about -29°C ; hence, we can reach pore sizes down to 2 nm when the porous media is saturated with water. However, a considerable advantage of the Peltier system is that the upper limit of resolution is of the order of 600 nm if we assume a temperature resolution of 0.1°C . Hence, we will plot all distributions in the range 2nm to $1\mu\text{m}$. To know the volume of water below 2 nm, we measure the amount of unfrozen water at -29°C as detailed below.

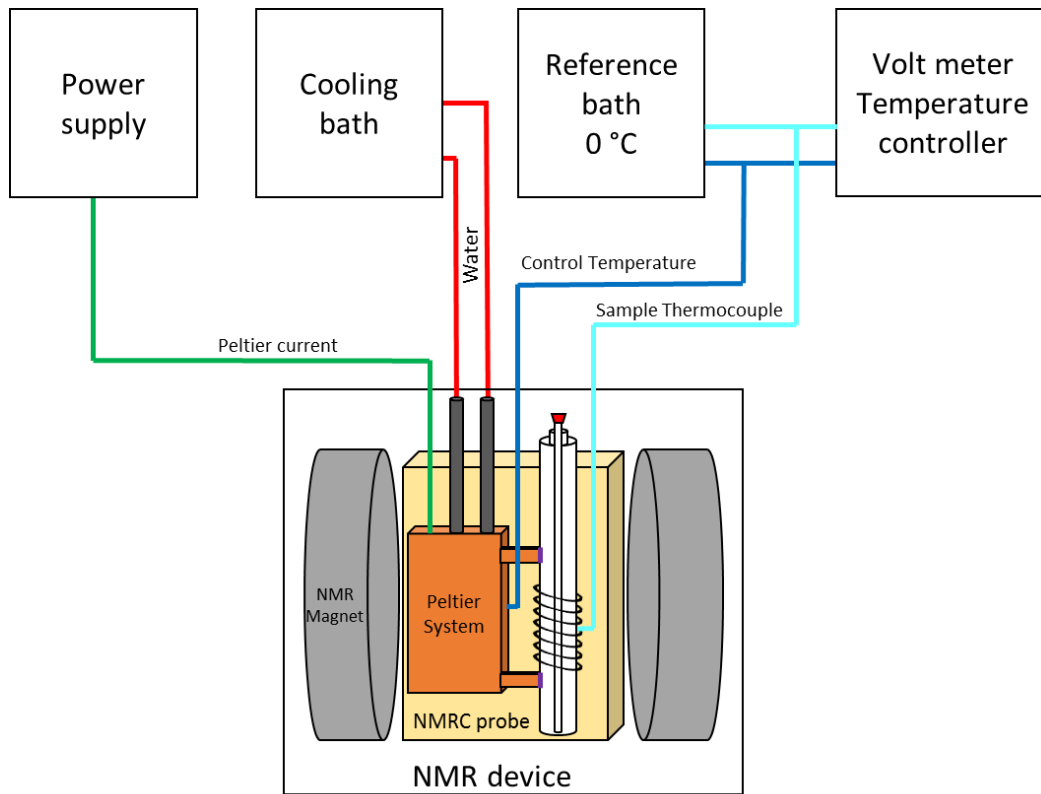


Figure 1 : Schematic of the IFPEN NMR cryoporometry system used in the study. Probe characteristics: 90° pulse duration = $1 \mu\text{s}$, minimum inter-echo time $TE_{\min} = 50 \mu\text{s}$.

In practice we varied the temperature as shown in Figure 2; at the beginning the temperature increase is large and gradually lowered when approaching the melting point at which the rate is about $0.002^\circ\text{C}/\text{min}$. Since a NMR measurement may take 2 minutes and temperatures are also averaged over 2 minutes, the corresponding NMR signal may be averaged over a temperature gradient of 0.004°C in the critical zone close to the melting point. From this principle, a theoretical resolution curve can be calculated as a function of pore size (Figure 2); for example, at 600 nm, the theoretical resolution is limited to about $\pm 11\text{nm}$ but is much smaller for pores less than 10 nm even though the temperature is increased much more rapidly.

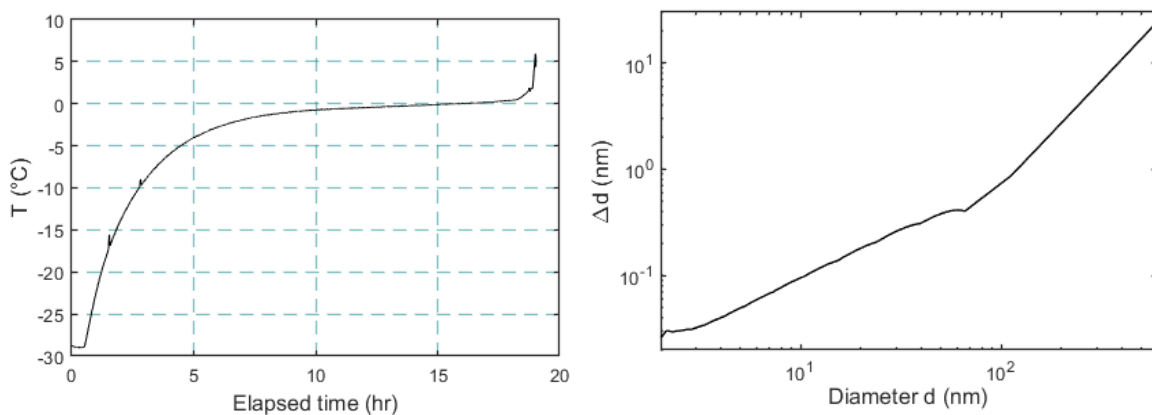


Figure 2: Typical temperature profiles during NMRC experiments (left). Temperature increase is reduced to $0.002^\circ\text{C}/\text{min}$ close to the bulk melting point (in this case water). Theoretical resolution assuming a measurement time of 120 s (right).

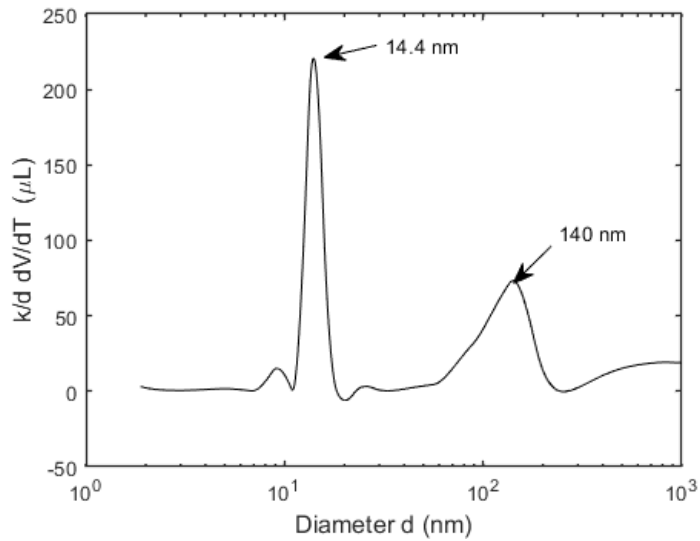


Figure 3 : Final checking of the cryoporometry set-up using a mixture of calibrated porous glass (BAM-PM-121 and BAM-PM-122 from European Reference Materials) with mean pore diameter of 15.3 ± 0.2 and 139.0 ± 3.7 nm.

Since temperature is only measured in the close vicinity of the sample, a small but unknown adjustment is necessary. This is performed by making a measurement using the above temperature ramp on a mixture of calibrated porous glass (BAM-PM-121 and BAM-PM-122 from European Reference Materials) containing two narrow cylindrical pore sizes (mean diameter of 15.3 ± 0.2 and 139.0 ± 3.7 nm). Using a linear correction in which a simple shift and a slope correction factor are introduced, we could match simultaneously both sizes with small errors (14.4 and 140 nm instead of 15.3 and 139.0 nm, Figure 3).

The amount of liquid in the sample was measured using a Hahn echo recorded at time $TE=0.3$ ms. It is a compromise such as to avoid detecting plastic ice while keeping the detection of the remaining liquid as high as possible. This is indeed a difficulty in natural tight porous system for which T_2 relaxation times are often very short, of the order of 1 ms for the water signal (Figure 4). The relaxation times of plastic ice in porous media were also unclear to us and to our knowledge are not available in literature. Hence, we measured a T_1 - T_2 map at -29°C on a water saturated alumina sample having pore sizes around 8 nm only, therefore containing no liquid phase at that temperature. The result is summarized in Figure 4 by a straight line located at $T_2 = 0.1$ ms and T_1 spanning essentially between 10 and 100 ms (the measured T_1 - T_2 map is very narrow along the T_2 axis and much wider along the T_1 axis). Assuming that such relaxation times are valid in all systems, we will detect a small residual solid signal when measuring the liquid signal with a Hahn echo at $TE=0.3$ ms. Indeed the magnetization decay of a T_2 component around 0.1 ms and measured at 0.3 ms is only reduced by 95% ($1 - \exp(-3)$).

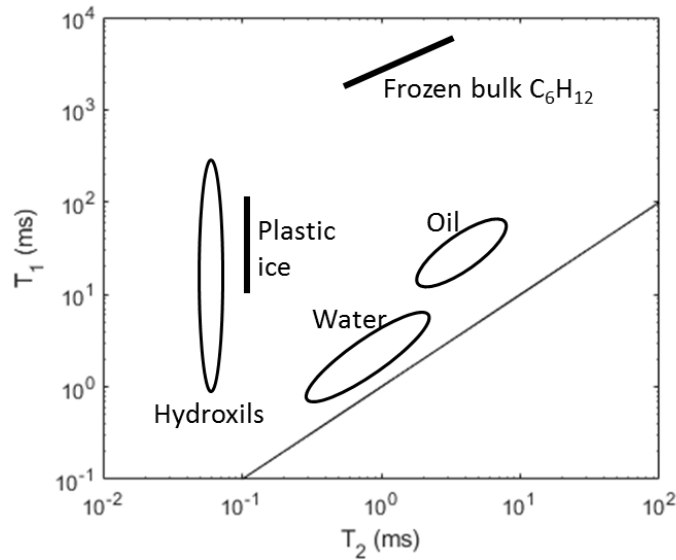


Figure 4 : Schematic of T_1 and T_2 relaxation times found in the systems studied, from literature and our own experience [21,22,30]. For bulk cyclohexane measured in this study, the values are valid in the temperature range between -30 up to 5 °C.

To evaluate the pore occupancy by water and oil, we first attempted to use cyclohexane as the hydrocarbon phase. It has indeed interesting properties in terms of melting temperature (6.5°C) and k_{GT} constant ($190 \text{ K}\cdot\text{nm}$), as well as wetting properties. Then to obtain the amount of liquid oil and water in equation 1, one can use T_1 - T_2 maps and take advantage of the higher T_1/T_2 ratio of hydrocarbon phases [21,22,30] compared to water (Figure 4). Hence, in theory, one could evaluate all components present in the system, from liquid to solid oil and water since frozen cyclohexane has also a distinct position in the T_1 - T_2 map (Figure 4, measured in the cryoporometry device). However, the numerous radio-frequency pulses necessary to perform these maps provoke a significant heating of the sample ($\sim 1^\circ\text{C}$) that cannot be compensated easily by the temperature regulation system. In fact, even a single T_2 relaxation measurement generates temperature fluctuations in the sample and only a Hahn and T_1 sequences are allowed; in addition on the T_1 axis, plastic ice and oil clearly overlap. Therefore we chose decane as the hydrocarbon phase as in Alnaimi et al. [27]; decane has a melting temperature lower than the lowest possible temperature in our system ($< -29^\circ\text{C}$) and will not interfere with the solid-liquid transition of the water in the presence of oil. Hence, we used the same protocol as in the fully saturated case (a Hahn echo at $TE=0.3 \text{ ms}$) and we were able to measure the pores occupied by water in the presence of oil. By comparison with the distribution at 100% water saturation, we can deduce the distribution of the pores occupied by oil.

2.2 NMR measurements

The cryoporometry probe described above is part of a low field Maran Ultra spectrometer from Oxford Instruments with a proton Larmor frequency of 23.7 MHz . It is specifically designed to have a low quality factor to be mostly insensitive to temperature variations down to -30°C . Hence, it has also short pulses and dead times such as the minimum achievable inter-echo time TE is $50 \mu\text{s}$. A typical signal recorded during NMRC experiments is shown in Figure 5; the NMR amplitude is the maximum of the recorded Hahn echo at $TE=0.3 \text{ ms}$. The curve is then fitted with MATLAB least square spline approximation function in order to obtain a smooth derivative of $V(T)$ (equation 2). T_2

measurements were performed with a CPMG sequence in which TE=50 μ s and T₁-T₂ maps were measured with a standard combined inversion recovery and CPMG sequence.

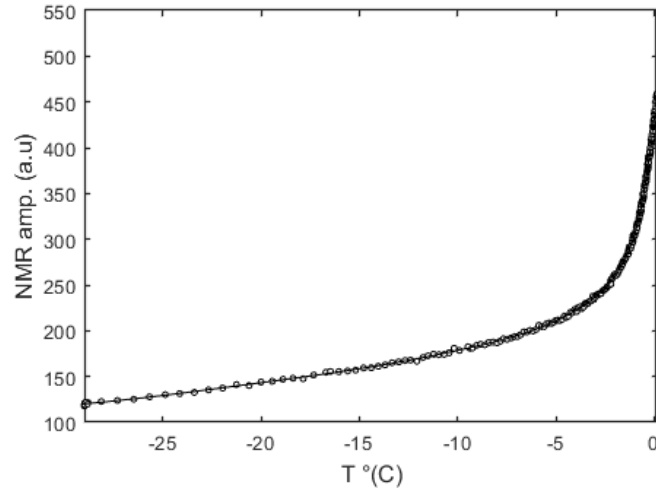


Figure 5 : Example of raw data recorded during NMRC experiments (open circles) on sample S3 at Sw=100% (Table 1). The line is a least square spline approximation used to calculate a smooth derivative dV/dT of the curve and produce the pore size distribution according to equation 2.

2.3 Diffusion measurements

We also performed D₂O diffusion exchange experiment to determine water diffusion coefficient and the amount of non-exchangeable water in the porous system [31–33]. In these experiments we record the ¹H concentration C vs. time when the sample is immersed into D₂O. We used however larger samples (10 mm) together with an 18 mm standard probe in the spectrometer. The recorded curve is then analyzed using well known analytical formulae. The solution of a diffusion equation in a cylinder of length $L=2l$ and radius $r=d/2$ is the product of two terms, C_{ps} and C_{cyl} , respectively representing the diffusion in a plane sheet (“ps”) and in an infinite cylinder (“cyl”), and are given by:

$$C = \frac{M(t_D)}{M(t_D = 0)} \quad (3)$$

$$C^* = \frac{M(t_D) - M(t_D = \infty)}{M(t_D = 0) - M(t_D = \infty)} = C_{ps} C_{cyl} \quad (4)$$

$$C_{ps} = \sum_{n=1}^{\infty} \frac{2\alpha(1+\alpha)}{1+\alpha+\alpha^2 p_n^2} \exp\left(-D_p p_n^2 \frac{t_D}{l^2}\right) \quad (5)$$

$$C_{cyl} = \sum_{n=1}^{\infty} \frac{4\alpha(1+\alpha)}{4+4\alpha+\alpha^2 q_n^2} \exp\left(-D_p q_n^2 \frac{t_D}{r^2}\right) \quad (6)$$

where p_n are the non-zero positive roots of the equation $\tan p_n = -\alpha p_n$, q_n the non-zero positive roots of the equation $\alpha q_n J_0(q_n) + 2J_1(q_n) = 0$, α is the volumetric D₂O/H₂O ratio, M is the measured NMR magnetization and t_D is the diffusion time. The pore diffusion coefficient D_p is

obtained by fitting the normalized curve C^* ; however we plot the data using C to highlight the asymptotic concentration at the end of the diffusion. More details can be found elsewhere [33].

2.4 SEM and STEM images

The structural characterization of the porosity was performed on the sample surfaces using a Scanning electron microscopy (SEM) Crossbeam 540 Zeiss, at a low acceleration voltage (1KV), without conductive coating. For these observations, the sample surface was polished in two steps. A first mechanical polishing was carried out using the Mecatech 234 polisher up to the $1/4\mu\text{m}$, then the final polishing was performed by Argon ion milling using the SEM mill Fischione 1060 apparatus at 4KV with beams angle of 2° (cycle of 30 minutes). Complementary observations were also performed in the transmission mode, using the additional Zeiss STEM (Scanning transmission electron microscopy) detector. This imaging mode, based on the collection of the transmitted or scattered electrons through a sample allows the observation of nanostructures in a SEM, with an optimal spatial resolution. In this configuration, an ultrathin lamella of less than 100nm thick, thinned to be transparent to electrons, is machined using a focused ion beam of gallium (FIB). The FIB preparation procedure consists in machining a cross sectional slice by coarse milling, extracting the slice from the sample using a micromanipulator and thinning the lamella by fine milling until the cross section is transparent to the electrons.

The samples used for the SEM characterization were taken close to the ones used for cryoporometry (see next section) and are considered as representative despite they were not realized on the samples themselves. The Vaca Muerta formation is known to have large zones in which the macroscopic properties do not vary much, and this is the case here.

2.5 Samples

Several samples originating from the Vaca Muerta formation [21,34,35] were used in this study. The starting point is the availability of large cores (not necessarily preserved) in which small cylinders are drilled for different purposes:

- cylinders of diameter 3.6 mm and length 20 mm for performing NMRC experiments,
- cylinders of diameter 10 to 15 mm and maximum length 20 mm for performing diffusion experiments [31,32],
- some pieces of rock a few millimeters in size for performing high resolution visualization and,
- a few tenth of grams of material for performing Rock-Eval® experiments [36,37]; during these experiments, a pyrolysis is performed with well-defined temperature ramps specifically designed to provide an assessment of free and/or sorbed hydrocarbons still present.

All samples indicated in Table 1 have been taken within a zone of a few centimeters in the large core and are considered representative of the same porous structure.

To obtain an initial 100% water saturation state, samples have been placed in a cell filled with deionized water and brought to a pressure of 100 bar during about 5 days. After saturation, the oil phase is introduced in the porous medium by simple immersion into decane (spontaneous drainage) yielding reasonably low water saturation values (Table 1). Here we take advantage of the oil-wetness of the Vaca Muerta samples [21]. After a first set of measurements (see Workflow in next section) the samples were cleaned with the objective of removing the fluids in place without altering the surfaces, and in particular the adsorbed long chain hydrocarbons responsible for the oil-wetness; it

was performed using a Soxhlet extractor first with isopropanol (3 days) followed by dichloromethane (4 days).

Table 1 : Samples characteristics and various experimental results. Saturation values (S_w) are given before cleaning. TOC: total organic content, VR: vitrinite reflectance. Porosity at -29°C before cleaning (b.c.) and after cleaning (a.c.) are given as a fraction of the total porosity. The non-exchangeable porosity obtained after the D_2O diffusion experiment is also given as a fraction of the total porosity.

Sample ID	L (mm)	D (mm)	Porosity (%)	S_w after spontaneous drainage	Porosity at -29°C b.c.	Porosity at -29°C a.c.	Non exch. porosity	TOC (%)	VR (% R_0)
S3	20.76	3.65	15.9	0.278	0.56	0.24	-	6.2	1.12
S5	19.95	3.67	14.1	0.254	0.60	0.34	-		
S6	14.85	11.95	14.6	-	-	-	0.19		

Porosities calculated from pore volumes and geometrical total volumes (Table 1) are in the expected range [21]. NMR pore volumes were obtained by taking all T_2 components larger than 0.2 ms, ignoring hydroxyls (Figure 6). Decane saturation is obtained by associating all T_2 components larger than 1 ms to oil; indeed decane has a clear signature with a higher T_1/T_2 ratio as expected and we could verify the disappearance of the water components after D_2O exchange (Figure 6). It is sufficient to use T_2 distribution alone to obtain pore volume and saturation although there exist a small signature of the organic matter at $T_1 \cong 80$ ms and $T_2 \cong 0.7$ ms (Figure 6) overlapping with the water components of the T_2 axis. For the geochemical properties, the Rock-Eval[®] analysis indicate a T_{max} (Sh2) value of 461°C and a low Hydrogen Index HI (Sh2) of 100 mgHC/gTOC, meaning that the sample reached the gas window thermal maturity.

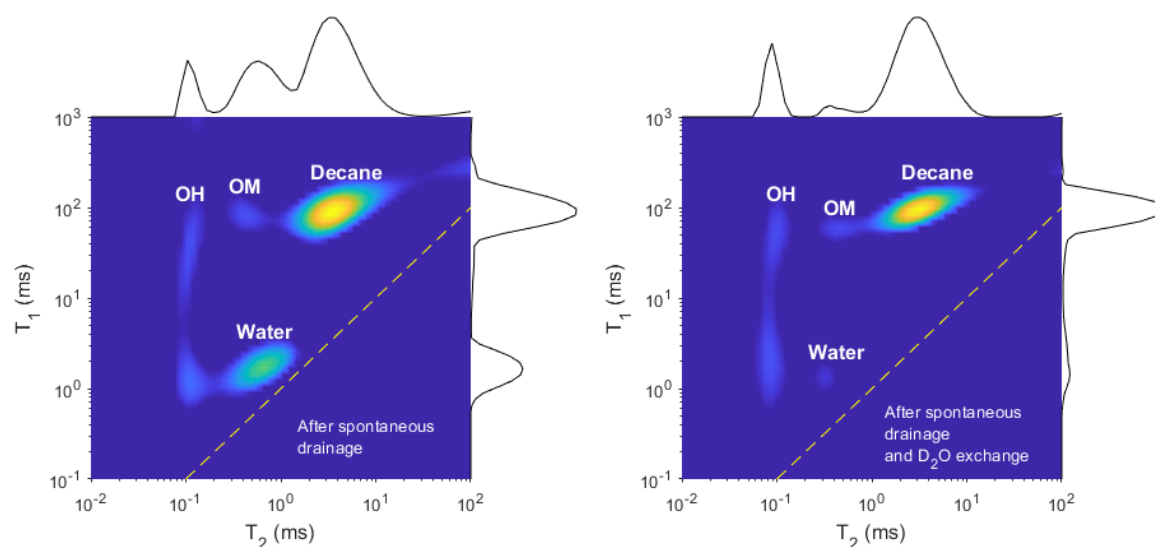


Figure 6 : T_1 - T_2 maps for sample S3 measured after spontaneous drainage with decane, and after exchange with D_2O . Decane has a clear signature with a higher T_1/T_2 ratio (~ 27) compared to water (~ 2.5) as expected. OM: organic matter, OH: hydroxyls. The dashed line indicates the ratio $T_1/T_2=1$.

2.6 Workflow

The general workflow of experiments and sample handling is depicted in Figure 7. The information provided by all experiments is the following:

- NMRC experiments at 100% water saturation and after spontaneous drainage by decane provide the main information of the pore occupancy of each phase,
- NMRC experiments after D₂O exchange provide the pore occupancy of non-exchangeable water in the presence of decane,
- the D₂O exchange experiment provides the effective water diffusion coefficient and the exchangeable water at 100% water saturation; with the knowledge of the diffusion coefficient, we obtain also the precise time scale for exchanging water by D₂O in any size of rock cylinders,
- high resolution imaging provides an important but qualitative visual proof of the existence of the pore sizes determined by NMRC experiments; in particular, a typical size of the organic and mineral pores, and the presence of bitumen or pyrobitumen for example,
- the Rock-Eval® Shale Play™ method provides the amount and maturity of the kerogen, as well as more information about the lighter hydrocarbons in place not detailed here.

Within the NMRC protocol, T₂ and T₁-T₂ maps were performed at -29°C before the temperature ramp to determine non frozen water (hence water located in pores smaller than about 2 nm), and at the end of the ramp when water is in a liquid state in all pores (at -29°C, a change of temperature of 1°C induce a low and non-measurable melting).

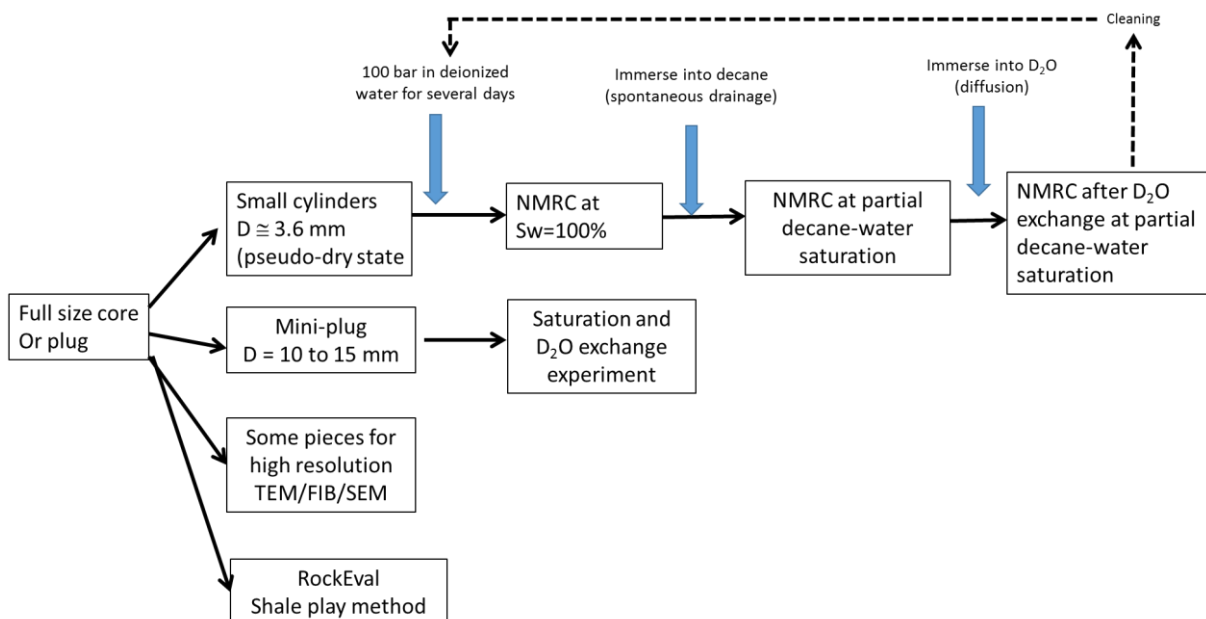


Figure 7 : General workflow including additional geochemical measurements such as Rock-Eval® Shale Play™ method.

3 Results

3.1 Pore size distribution by cryoporometry

The pore size distributions (PSD) on sample S3 at 100% water saturation and partial water saturation are shown in Figure 8. At $Sw=100\%$, the PSD is mainly bimodal with modes around 2 and 80 nm. As mentioned above, the PSD only expresses the amount of melted fluid as a function of temperature. Hence when the distribution still contains significant amplitudes close to the minimum resolved pore size (2 nm), one should suspect the existence of pores smaller than 2 nm. Indeed, the amount of unfrozen liquid measured separately and described later confirms this suspicion. At $Sw=27.8\%$, the peak around 80 nm is no more present while the one around 2 nm is nearly the same. Hence we can deduce the pore occupancy of decane by making the difference between the water PSD's obtained at $Sw=100\%$ and $Sw=27.8\%$. Around 2 nm, the negative amplitudes due to uncertainties when making the signal derivatives have been set to zero. Similar results are obtained on sample S5 (Figure 8). In this case, we have chosen to show the results obtained after cleaning.

When considering all PSD measured before and after cleaning, and after D_2O exchange (Figure 9) following the workflow described in Figure 7, we can conclude that the cleaning has a minor effect except for the amount of unfrozen liquid discussed later. Both at $Sw=100\%$ and after spontaneous drainage, the PSD are similar. On one hand, this is expected because the solvents used for cleaning are not able to remove the organic compounds adsorbed on the surface. On the other hand, an uncleaned sample originating from an un-preserved core exposed to air may contain residual hydrocarbon components that must be removed to properly determine PSD. However, this is not likely the case since our samples reached the gas window. Of special interest also is the PSD measured after spontaneous drainage and D_2O exchange; the non-exchangeable water left in the porous system and generating a measurable signal is located in the smallest pores around 2 nm. The existence of non-exchangeable water is also seen in the fully monitored D_2O exchange experiment described below.

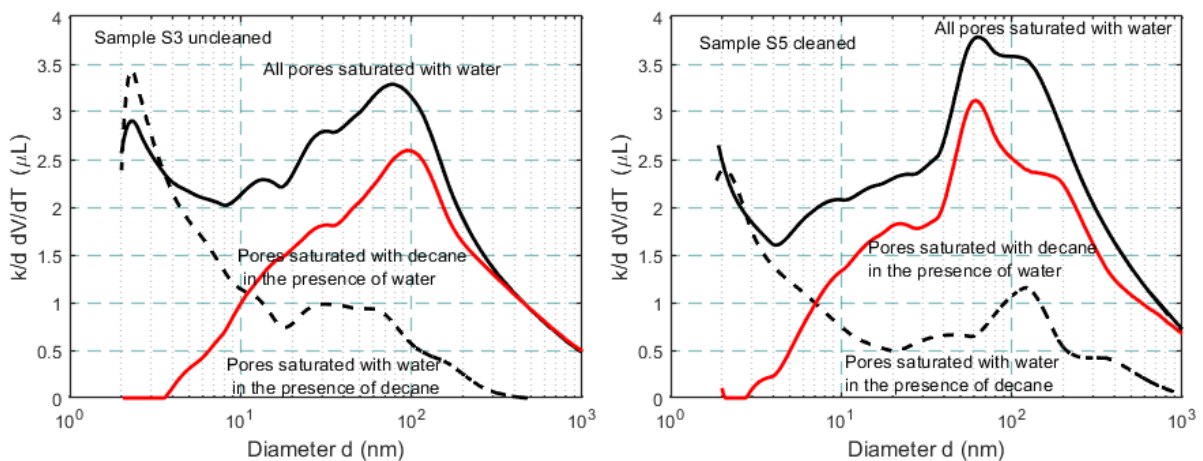


Figure 8 : Pore occupancy of water and decane at $Sw=100\%$ (full line) and after spontaneous drainage (dashed line) for sample S3 (no cleaning, $Sw=27.8\%$) and S5 (after cleaning, $Sw=25.4\%$). The distribution for decane is obtained by difference of the two PSDs (full red line).

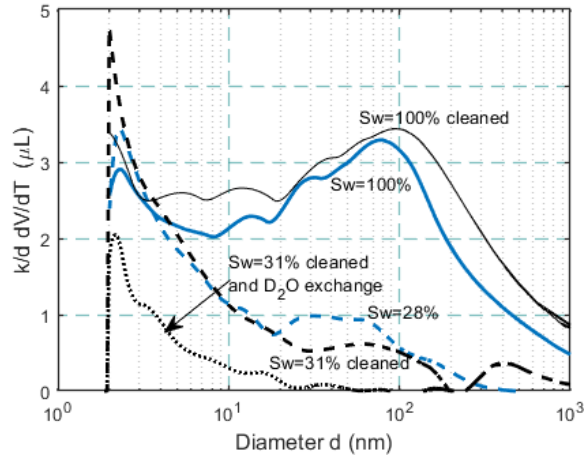


Figure 9 : PSD measured at each step of the workflow presented in Figure 7 for sample S3. Blue curves: as received (uncleaned) sample, black curves: cleaned sample. Full lines: 100% water saturation, dashed lines: in the presence of decane, short dashed line: after D₂O exchange.

3.2 Water volume below 2 nm and non-exchangeable water

The amount of non-frozen liquid is determined using a T_2 measurement performed at the lowest achievable temperature of -29°C , corresponding to pore sizes smaller than 2 nm (see an example in Figure 10). The temporary heating induced by the CPMG sequence has little consequence at this temperature as no significant water volume is melted. We observed a significant amount of non-frozen liquid, corresponding to T_2 components larger than 0.2 ms. After correction by a Curie law, the measured volumes represent a large fraction of the total porosity, up to 0.60 (Table 1). After cleaning, the unfrozen porosity fraction decreases by a factor of 2. Such large fractions are surprising, but we could verify that the volumes measured during cryoporometry experiments (melted volume) added to the volumes below 2 nm were consistent with the total pore volumes measured with T_2 distribution at 7°C . It is noteworthy that, in the un-cleaned state, the porosity fraction of pores below 2 nm (on average 0.58) is larger than the fraction of water after spontaneous decane displacement (on average 0.26). Hence we have to conclude most likely that a significant fraction of the organic matter is filled with oil in pores smaller than 2 nm and not detected by our (differential) cryoporometry technique. This is however not the case after cleaning, meaning that the cleaning process might have an effect on the smallest pores of the organic matter.

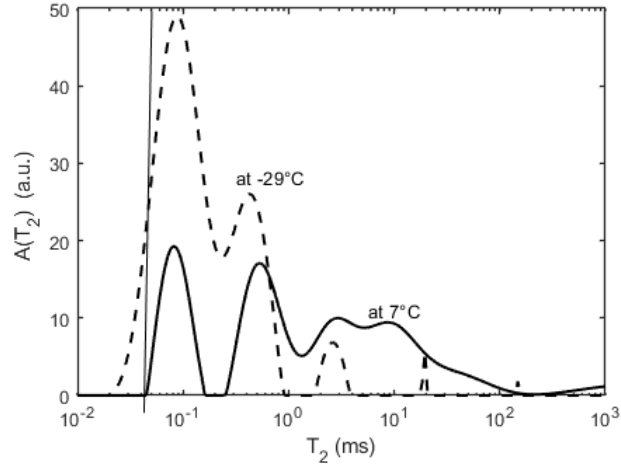


Figure 10 : T_2 distributions for sample S3 measured at 7°C (full line) and at -29°C (dashed line) before the NMRC experiment ($S_w=100\%$). The vertical line indicates the lowest resolved relaxation time.

A fully monitored diffusion experiment has been performed on sample S6. The recorded ^1H dimensionless concentration C vs. time when the sample is immersed into D_2O at a constant temperature of 30°C is shown in Figure 11. After fitting, we obtain an effective diffusion coefficient $D=1.1 \cdot 10^{-10} \text{ m}^2/\text{s}$. We can deduce a tortuosity D_m/D of 23.6 where D_m is the bulk water diffusion coefficient at 30°C ($D_m=2.60 \cdot 10^{-9} \text{ m}^2/\text{s}$). Using an Archie type model, $D/D_m = \Phi^{m-1}$, we find $m= 2.64$. With such diffusion coefficient also found in other cases [22], the typical diffusion length at $t=1\text{ms}$ (\sim the lowest T_2) is of the order of 800 nm much larger than most pore sizes. Hence the porous system is in principle highly coupled by diffusion [26,38] during T_2 magnetization decay and T_2 distributions cannot represent true pore size distributions. At the extreme case of coupling, a single peak could be observed but in practice the T_2 distribution still has a width of about 1 decade most likely due to heterogeneities as a scale larger than the diffusion length; for example in shales not containing organic matter and studied in the context of nuclear waste storage [39], the T_2 distribution transformed into a pore size distribution using a surface relaxivity value appeared in disagreement with multi-scale image analysis. In the present situation, it is surprising to observe a wide T_2 distribution (Figure 10, about 2 decades on sample S3) compared to the pore size determined by cryoporometry (Figure 8, about 3 decades on sample S3). The explanation is most likely that there exist two pore networks with different surface relaxivities, presumably the mineral and organic ones, therefore inducing a T_2 contrast and widening the distribution.

Beside the diffusion coefficient, the quantity of interest is the amount of non-exchangeable water obtained from the asymptotic ^1H concentration C_f (Figure 11, horizontal line). We measured $C_f=0.28$ whereas the residual value obtained by dilution (uniform concentration inside and outside the sample) should be $V_{\text{H}_2\text{O}}/(V_{\text{H}_2\text{O}}+V_{\text{D}_2\text{O}})=0.088$ when all water is exchangeable. Hence the non-exchangeable porosity is $\Phi_{\text{NE}}= \Phi (0.28-0.088) = 2.8 \text{ p.u.}$ (porosity units, 19% of the total porosity). For practical purpose, we can also deduce the typical time needed to exchange water by deuterium in smaller cylinders typically used for NMRC experiments. At 100% water saturation (i.e. $D=1.1 \cdot 10^{-10} \text{ m}^2/\text{s}$), less than 10 hours are necessary. At a lower saturation (i.e. assuming for example $D=1.1 \cdot 10^{-11} \text{ m}^2/\text{s}$, 10 times smaller), a few days are necessary (80 hours). These durations were used in the workflow of Figure 7.

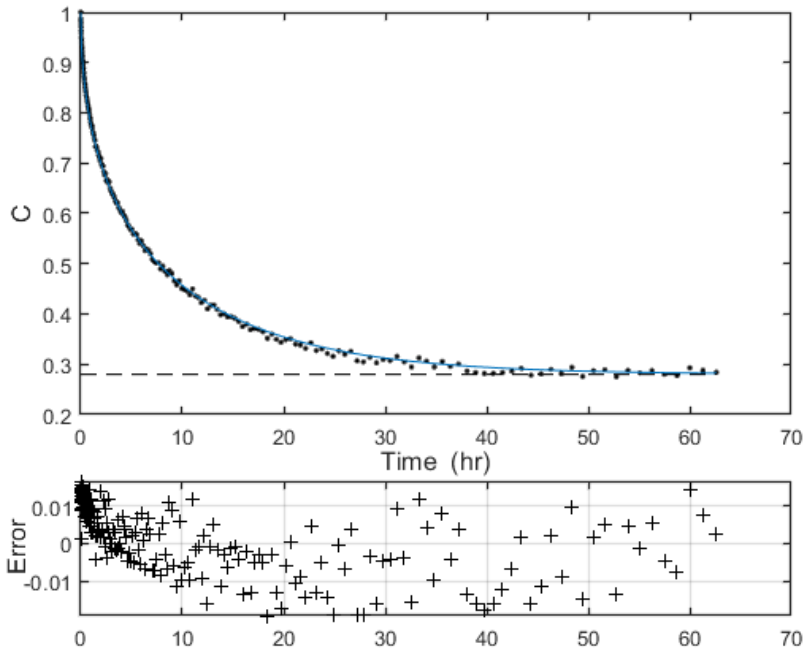


Figure 11 : Diffusion experiment on sample S6. The line indicates the fitted diffusion model yielding a pore diffusion coefficient $D=1.1 \cdot 10^{-10} \text{ m}^2/\text{s}$ at 30°C . The volume of D_2O is 2.5 ml and the pore volume is 0.241 ml. The asymptotic concentration is $C_f=0.280$ (horizontal dashed line). The lower panel indicates the difference between the diffusion model and the data.

3.3 Microscopy observations

The purpose of these observations is to qualitatively confirm the existence of pores as determined by cryoporometry experiments. We selected here two images among many representing the most important observations. An overview at a field of view of about $40 \mu\text{m}$ of the inorganic and organic components is first given in Figure 12. We retrieve globally the typical structure found not only in the Vaca Muerta formation in Argentina [34,40,41] but also in the Barnett [4] or Dalong formations [10] with however significant variations induced by the maturity; here we have large patches of porous organic matter with a “sponge like” aspect inserted into a mineral matrix composed of quartz or mixture of quartz, albite and calcite. Clays are visible either filling large pores but also mixed within the organic matter as will be seen later. Pyrite with its typical framboidal aspect is also clearly visible (Figure 12). When visualizing specifically the porous structure of the organic matter (Figure 13), one finds qualitatively others pores of smaller size suggesting a large pore size distribution ranging from the micron-scale down to tens of nanometer. The range could also extend further down as it has been shown that organic matter can also have a connected pore network at the nanoscale [8]. Therefore, we associate the 80 nm mode of the distribution measured either at 100% water saturation or in the presence of decane (Figure 8) with the porous organic matter network. It is also presumably responsible of the oil-wetness characteristics of the samples and thus decane can penetrate this porosity fraction without the need of any pressure.

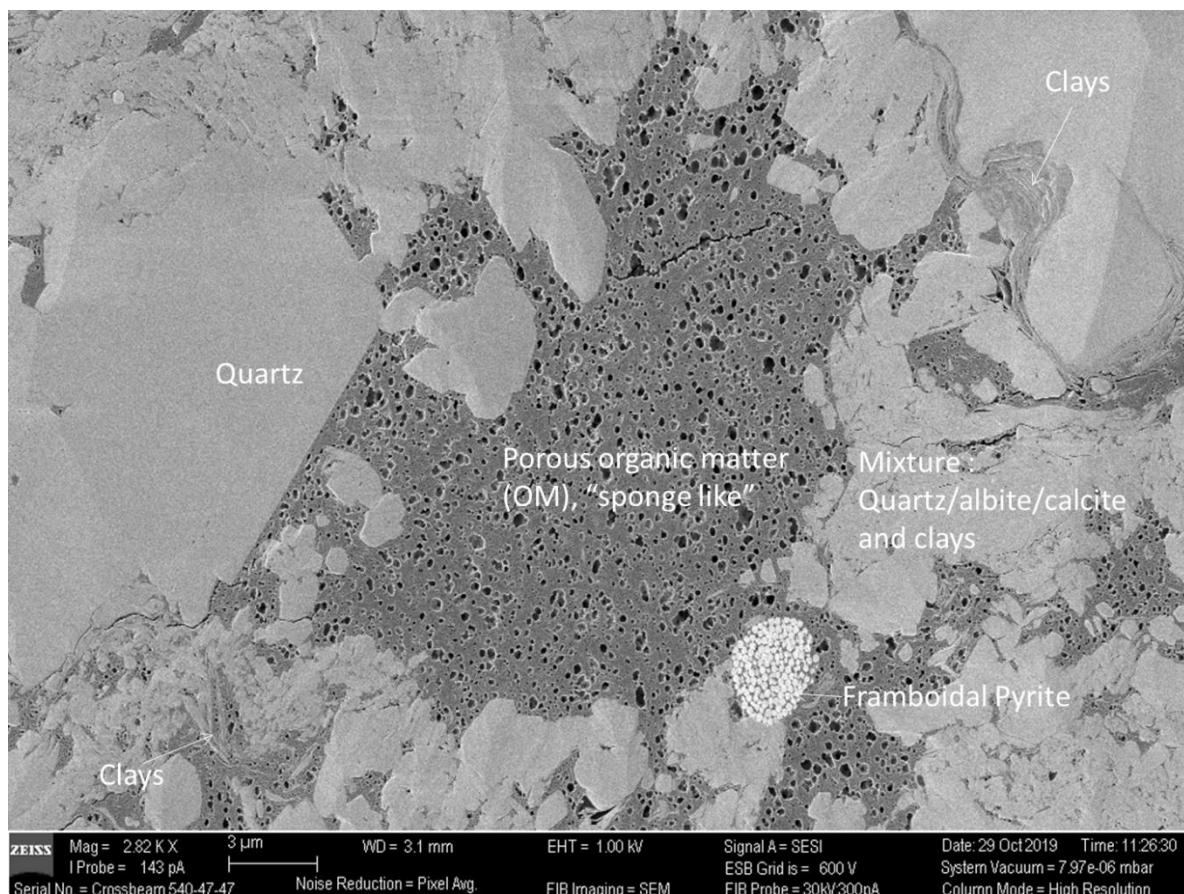


Figure 12 : Overview of the structure of the samples studied (SEM technique). Image width: 40 μm .

The qualitative association of pore filled with water is a more difficult task. First the volume amount of pores below 2 nm is quite large (58% on average) and is out of reach of the present imaging techniques. There exist three main possibilities at the nanoscale, all detectable by NMR relaxation: water associated with clays and especially smectite [42], water associated with calcite, and possibly water in the smallest pores of the organic matter and not invaded by decane. Concerning clays, we observe that they are also present as dispersed and intimately mixed with organic matter (Figure 13) besides lining mineral surfaces (Figure 12). Hence, we can suspect that part of the clay porous network is not well connected, potentially explaining the significant amount of non-exchangeable water during the D_2O diffusion experiment. A more detailed study would be required to establish a link with mineralogical information such as clay content and illite/smectite fraction, and organic matter content. But this is out the scope of this study and will be the object of future work.

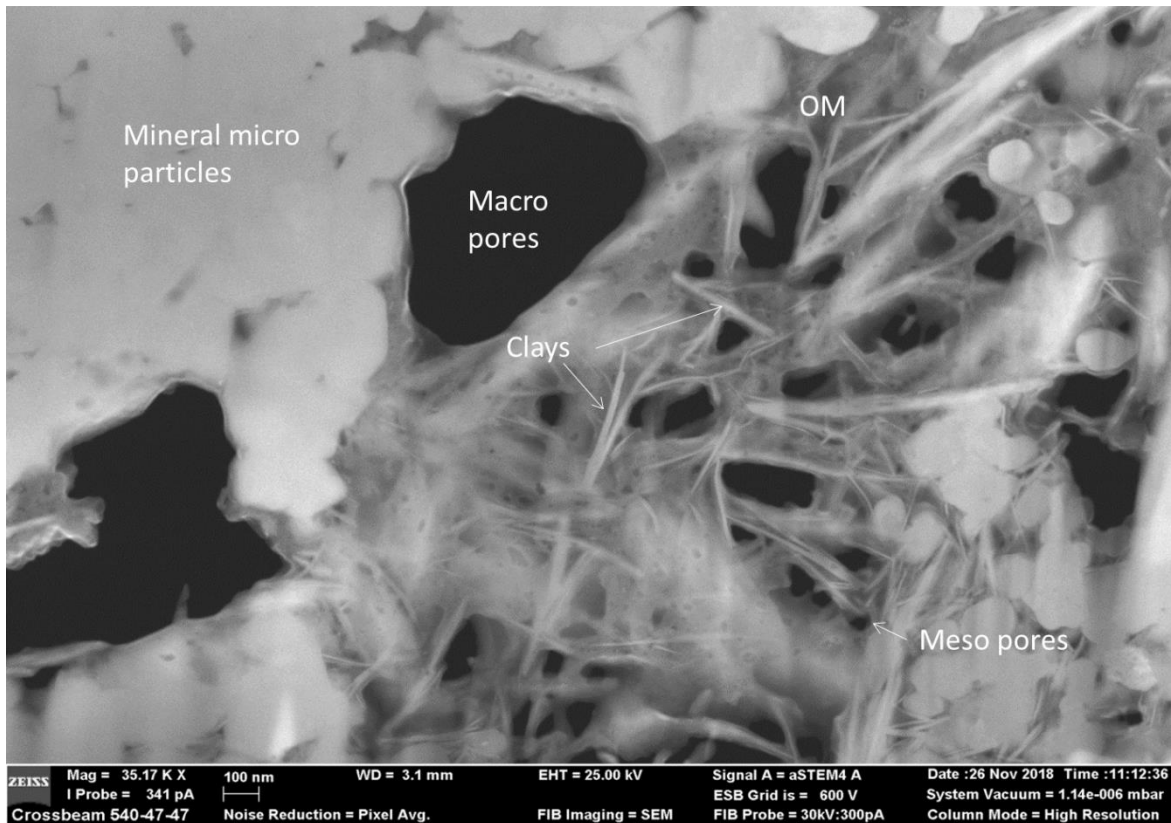


Figure 13 : Detailed view of the organic matter close to mineral particles (STEM technique). OM: Organic Matter

4 Summary and conclusion

The NMR cryoporometry technique (NMRC) in single phase saturation allows the measurement of pore size distribution in the range [2-600 nm] with the device used in this study ($T > -29^{\circ}\text{C}$). We used this technique together with relaxation measurements to establish a workflow to determine the pore occupancy of water and oil in samples originating from the Vaca Muerta formation. Since the samples are oil-wet, it was possible to introduce oil by simply immersing fully water saturated samples into oil yielding oil saturation as large as 70%. The chosen oil phase is decane, a liquid that does not freeze until -29°C .

The workflow includes:

- NMRC experiments at 100% water saturation, after spontaneous drainage with decane, and after D_2O exchange,
- D_2O exchange experiments to obtain the amount of non-exchangeable water and the precise time scale for full exchange,
- T_2 and T_1 - T_2 map measurements to provide precise determination of water saturation and unfrozen liquids at -29°C ,
- Rock-Eval[®] Shale Play[™] pyrogram to evaluate maturity and the presence of low molecular weight hydrocarbons,
- Pore structure visualization.

At 100% water saturation, the measured PSD indicates two main peaks around 2 and 80 nm. After spontaneous drainage, the pores occupied by water in the presence of decane are mostly around 2

nm. The pore sizes occupied by decane in the presence of water can then be deduced by subtracting the distributions obtained at 100% water saturation and after spontaneous drainage (Figure 8). Oil is mainly located in pores around 80 nm.

From D₂O diffusion experiments at 100% water saturation, we observed that about 19% of the total porosity is non-exchangeable with D₂O. Moreover, from the measurements of the liquid signal at -29°C, we observed that on average 58% of the total porosity is still liquid and therefore located in pores below 2 nm, a significant amount. High resolution SEM and STEM images allow to associate most of the oil in the porous organic matter network whereas an ambiguity remains about the location of water presumably not only located in clays.

Acknowledgments: we would like to thank Dr. B. Webber for various discussion about the cryoporometry technique. Many thanks also to Dr. M. Romero-Sarmiento for providing the geochemical analysis. We had also useful discussion with Dr. N. Chanut and R. Pellenq about the porous structure in shales.

5 References

- [1] Q. Wang, R. Li, *Renewable and Sustainable Energy Reviews* 74 (2017) 715–720.
- [2] M. Tan, K. Mao, X. Song, X. Yang, J. Xu, *Journal of Petroleum Science and Engineering* 136 (2015) 100–111.
- [3] C.R. Clarkson, J.L. Jensen, S. Chipperfield, *Journal of Natural Gas Science* 8 (2012) 9–33.
- [4] Loucks, R. G., Reed, R. M., Ruppel, S. C., Jarvie, D. M., *Journal of Sedimentary Research* 79 (2009) 848–861.
- [5] C.R. Clarkson, N. Solano, R.M. Bustin, A.M.M. Bustin, G.R.L. Chalmers, L. He, Y.B. Melnichenko, A.P. Radliński, T.P. Blach, *Fuel* 103 (2013) 606–616.
- [6] S. Bernard, B. Horsfield, H.-M. Schulz, R. Wirth, A. Schreiber, N. Sherwood, *Marine and Petroleum Geology* 31 (2012) 70–89.
- [7] Y. Wang, J. Pu, L. Wang, J. Wang, Z. Jiang, Y.-F. Song, C.-C. Wang, Y. Wang, C. Jin, *Fuel* 170 (2016) 84–91.
- [8] J. Berthonneau, A. Obliger, P.-L. Valdenaire, O. Grauby, D. Ferry, D. Chaudanson, P. Levitz, J.J. Kim, F.-j. Ulm, R.J.-M. Pellenq, *Proceedings of the National Academy of Sciences of the United States of America* 115 (2018) 12365–12370.
- [9] R. Denoyel, P. Llewellyn, I. Beurroies, J. Rouquerol, F. Rouquerol, L. Luciani, *Part. Part. Syst. Charact.* 21 (2004) 128–137.
- [10] L. Xu, J. Zhang, J. Ding, T. Liu, G. Shi, X. Li, W. Dang, Y. Cheng, R. Guo, *Minerals* 10 (2020) 72.
- [11] Y. Zhao, L. Peng, S. Liu, B. Cao, Y. Sun, B. Hou, *Marine and Petroleum Geology* 102 (2019) 116–125.
- [12] J. Strange, M. Rahman, E. Smith, *Physical review letters* 71 (1993) 3589–3591.
- [13] M. Fleury, R. Fabre, Webber, J. B W, *Proceeding of the International Symposium of the Society of Core Analysts* (2015).
- [14] Webber, J. Beau W., P. Corbett, K.T. Semple, U. Ogbonnaya, W.S. Teel, C.a. Masiello, Q.J. Fisher, J.J. Valenza, Y.-Q. Song, Q. Hu, *Microporous and Mesoporous Materials* 178 (2013) 94–98.
- [15] B. Zhou, Q. Han, P. Yang, *Energy Fuels* 30 (2016) 9122–9131.
- [16] Webber, J. Beau W., P. Corbett, K.T. Semple, U. Ogbonnaya, W.S. Teel, C.a. Masiello, Q.J. Fisher, J.J. Valenza, Y.-Q. Song, Q. Hu, *Microporous and Mesoporous Materials* 178 (2013) 94–98.
- [17] J. Mitchell, J. Webber, J. Strange, *Physics Reports* 461 (2008) 1–36.
- [18] O.V. Petrov, I. Furó, *Progress in Nuclear Magnetic Resonance Spectroscopy* 54 (2009) 97–122.
- [19] Y.-Q. Song, R. Kausik, *Progress in Nuclear Magnetic Resonance Spectroscopy* 112-113 (2019) 17–33.
- [20] E.S. Kazak, A.V. Kazak, *Journal of Petroleum Science and Engineering* 183 (2019) 106301.
- [21] B. Nicot, N. Vorapalawut, B. Rousseau, L.F. Madariaga, G. Hamon, J.-P. Korb, ., *Petrophysics* 57 (2016) 19–29.
- [22] M. Fleury, M. Romero-Sarmiento, *Journal of Petroleum Science and Engineering* 137 (2016) 55–62.
- [23] Ozen A. E., Sigal R. F., *Petrophysics* 54 (2013).
- [24] S. Su, Z. Jiang, X. Shan, Y. Zhu, P. Wang, X. Luo, Z. Li, R. Zhu, X. Wang, *Journal of Petroleum Science and Engineering* 169 (2018) 309–316.
- [25] J.-P. Korb, B. Nicot, I. Jolivet, *Microporous and Mesoporous Materials* 269 (2018) 7–11.
- [26] K.E. Washburn, J.E. Birdwell, *Journal of Magnetic Resonance* 233 (2013) 17–28.

- [27] S.M. Alnaimi, J. Mitchell, J.H. Strange, Webber, J. B. W., *The Journal of Chemical Physics* 120 (2004) 2075–2077.
- [28] Y. Liu, Y. Yao, D. Liu, S. Zheng, G. Sun, Y. Chang, *Marine and Petroleum Geology* 96 (2018) 591–601.
- [29] Webber, J. B W, *Progress in Nuclear Magnetic Resonance Spectroscopy* 56 (2010) 78–93.
- [30] S. Khatibi, M. Ostadhassan, Z.H. Xie, T. Gentzis, B. Bubach, Z. Gan, H. Carvajal-Ortiz, *Fuel* 235 (2019) 167–177.
- [31] P. Berne, P. Bachaud, M. Fleury, *Oil & Gas Science and Technology – Revue de l’Institut Français du Pétrole* 65 (2009) 473–484.
- [32] M. Fleury, G. Berthe, T. Chevalier, *Magnetic Resonance Imaging* (2018).
- [33] M. Fleury, T. Chevalier, G. Berthe, W. Dridi, M. Adadji, *Construction and Building Materials* 259 (2020) 119843.
- [34] M.-F. Romero-Sarmiento, S. Ramiro-Ramirez, G. Berthe, M. Fleury, R. Littke, *International Journal of Coal Geology* 184 (2017) 27–41.
- [35] F. Rodriguez Monreal, H.J. Villar, R. Baudino, D. Delpino, S. Zencich, *Marine and Petroleum Geology* 26 (2009) 590–605.
- [36] M.-F. Romero-Sarmiento, D. Pillot, G. Letort, V. Lamoureux-Var, V. Beaumont, A.-Y. Huc, B. Garcia, *Oil & Gas Science and Technology – Revue d’IFP Energies nouvelles* 71 (2016) 37.
- [37] M.-F. Romero-Sarmiento, J.-N. Rouzaud, S. Bernard, D. Deldicque, M. Thomas, R. Littke, *Organic Geochemistry* 71 (2014) 7–16.
- [38] M. Fleury, J. Soualem, *Journal of Colloid and Interface Science* 336 (2009) 250–259.
- [39] Y. Song, C.A. Davy, D. Troadec, A.-M. Blanchenet, F. Skoczylas, J. Talandier, J.C. Robinet, *Marine and Petroleum Geology* 65 (2015) 63–82.
- [40] L.C. Crousse, S. Cuervo, D. Vallejo, L. Mosse, T. Fischer, D. McCarty, in: *Proceedings of the 3rd Unconventional Resources Technology Conference*, American Association of Petroleum Geologists, Tulsa, OK, USA, 2015.
- [41] A. Cavelan, M. Boussafir, O. Rozenbaum, F. Laggoun-Défarge, *Marine and Petroleum Geology* 103 (2019) 331–350.
- [42] M. Fleury, E. Kohler, F. Norrant, S. Gautier, J. M'Hamdi, L. Barré, *Journal of Physical Chemistry C* 117 (2013) 4551–4560.